Pervasive inter-individual differences in the sensorimotor-association axis of cortical organization

G. Bignardi[1,2], M.G. Nivard[3], H. L. Schaare[4,5], B. C. Bernhardt[6], R.A.I. Bethlehem[7,8], S. E. Fisher[1,9], & S. L. Valk[4,5,10*]

[1]Language and Genetics Department, Max Planck Institute for Psycholinguistics, Nijmegen, The Netherlands; [2]Max Planck School of Cognition, Leipzig, Germany; [3]Department of Biological Psychology, Faculty of Behaviour and Movement Sciences, VU University, Amsterdam, The Netherlands; [4] Max Planck Institute for Human Cognitive and Brain Sciences, Leipzig, Germany; [5] Research Center Jülich, Institute for Neuroscience and Medicine (INM-7), Germany; [6]McGill University, Montreal, Canada; [7]Autism Research Centre, Department of Psychiatry, University of Cambridge, Cambridge, United Kingdom; [8]Department of Psychology, University of Cambridge, Cambridge, United Kingdom; [9]Donders Institute for Brain, Cognition and Behaviour, Radboud University, Nijmegen 6500 HB, The Netherlands; [10]Heinrich-Heine-Universitaet Duesseldorf, Germany.

Abstract

Structural variation along a sensorimotor-association (S-A) axis is thought to scaffold intrinsic functional differentiation and, ultimately, cognition. Using structural equation modeling and a multivariate twin design, we reveal that group-level associations in the S-A axis can mask pervasive inter-individual differences. Despite theoretical models and group-level relationships between cortical microstructure and intrinsic function, we find instead individual-level differences in regional cortical network geometry of genetic and environmental origins to support the intrinsic functional organization of the human cortex.

Main

The human brain supports perception, action, as well as abstract cognition that is decoupled from immediate environmental input [1,2]. This diversity of functions is supported by the structural organization of the cortical mantle, reflected by the gradual dissociation between primary unimodal sensory and transmodal association cortical regions (S-A axis [3]) as a function of a vast array of neurobiological properties, including microstructural variation (myelination and cytoarchitecture) and inter-areal connectivity distance [3,4]. Here sensory areas show high microstructural differentiation, high myelination, and short-range connections, whereas association areas show less differentiated microstructural profiles, reduced myelination, and a combination of short-and long-range connectivity profiles [5–7]. As such, the structural organization along the S-A axis [1,8–10], provides a scaffold for functional differentiation [11,12], which in turn supports cognitive and behavioural flexibility [1,11].

Recent work enhanced our understanding of the link between group average macroscopic structural features, from microarchitectonic differentiation [13] to cortical geometry [14], and intrinsic functional features of the cortical mantle [11,15]. Notwithstanding well-documented associations at the group-level [3,4,8,16], whether inter-individual differences follow parallel trends is still poorly understood. To address this issue, we decomposed the deceptively straightforward question of whether the S-A axis's structural and functional properties correlate. First, we confirmed that the group average structural S-A axis's properties correlate with the group-level functional hierarchy. We then asked whether widely reported group averages can mask S-A axis associations at the level of the individual. Specifically, we tested whether individual regional cortical microstructure [8] and intrinsic network topology, captured by the geodesic distance of inter-connected regions across the cortical mantle [1], constrain the well-known functional dissociations between sensory and transmodal areas.

We combined microstructural and resting-state functional MRI data from the Human Connectome Project (HCP [17]; n=591 adults; 295 women, mean age 28 y; 22-37 y) and computed two structural metrics indexing S-A; microstructural profiles and cortical network geometry. First, in line with Burt et al. [8], we quantified regional microstructural profiles indexing the differentiation between sensory and transmodal areas using the individuals' mean intensity of regional T1w/T2w (T1w/T2w$_{mi}$) in 400 parcels [18]. Second, we quantified regional cortical network geometry by computing the geodesic distance (GD) between every cortical region and its corresponding functional network, averaged within each region to get parcel-wise estimates [1]. Last, we quantified individuals' functional S-A axis by obtaining the first component of the individual Functional Connectomes (FC) using diffusion map embedding (FC$_{G1}$, see methods) [1,19,20].

Group-level averaged maps of T1w/T2w$_{mi}$, GD, and FC$_{G1}$ (Fig. 1A-C) resembled previously published results [1,3,8,11]. T1w/T2w$_{mi}$, GD, and FC$_{G1}$ were moderately to strongly correlated with each other and mapped inversely to Yeo-Krienen 7 resting-state functional networks (Spearman ρ=-.61 and ρ=.75 between T1w/T2w$_{mi}$ and FC$_{G1}$, and GD and FC$_{G1}$, respectively; all p<.001; Fig. 1D-E; see Fig. S1). However, group-level maps masked widespread individual regional variability (Fig. 1F), which, in contrast to other neurobiological properties [3], covaried weakly, yet significantly, with the S-A axis itself (Spearman ρ=-.18, p<.001, ρ=.13, p=.01, and ρ=.37, p<.001, for σ^2FC$_{G1}$, σ^2MP and σ^2GD, respectively). Crucially, group-level associations did not align with regional individual-level associations (Fig. 1G). Indeed, when focusing on individual regional S-A axis variability (Fig. 1H), only less than 4% of regional associations between T1w/T2w$_{mi}$ and FC$_{G1}$ survived significance testing, in contrast with 58% of regional associations between GD and FC$_{G1}$ (all passing Bonferroni corrected p; similar trends were observed with unaligned individual FC$_{G1}$, see Fig. S2). These results suggest that, when shifting the focus from group-level to individual-level associations, regional cortical network geometry, rather than microstructure, predominantly explains functional S-A axis variability.

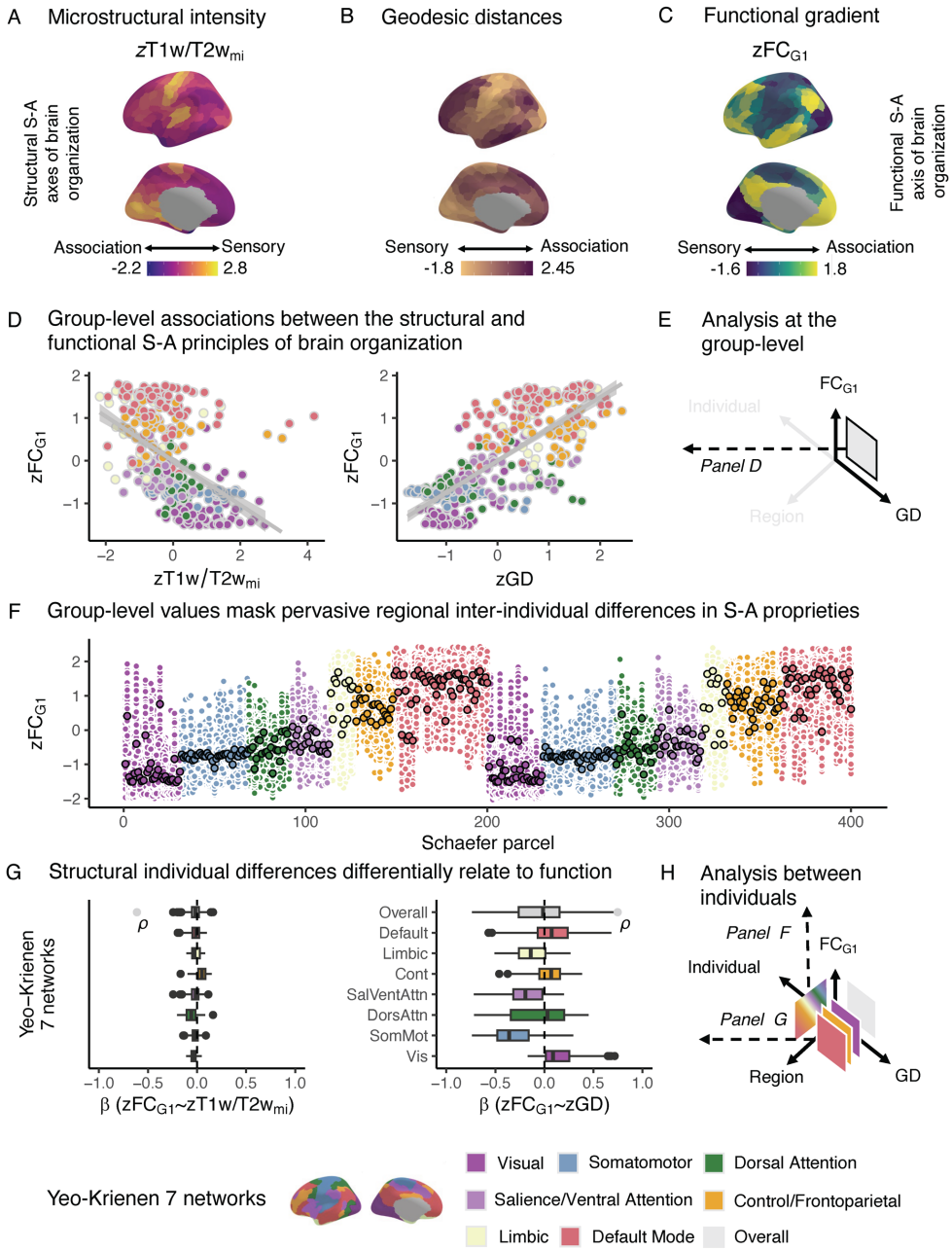

Figure 1. *Group-level trends in structural and functional S-A axis mask individual-level differences*. **A** Z-scores of the mean microstructural intensity ($T1w/T2w_{mi}$) averaged intra-individually across profiles and inter-individually across parcels. **B** Z-score of the Geodesic Distances (GD) averaged inter-individually across parcels. **C** Z-scored sensorimotor-association axis (S-A) functional gradient (FC_{G1}) extracted from the averaged Functional Connectome across individuals. **D** Scatter plots show the relationship between Z-scored parcel-wise values of structural S-A axes (x-axis) and FC_{G1} (y-axis). Each dot represents one parcel. The colours represent Yeo-Krienen 7 network. **E** Representation of group-level analytical dimensions. Both regional and individual differences are lost in favour of average trends. **F** Group-level (black contour) and individual-level (white contour) standardised FC_{G1} parcel-wise estimate. **G** Boxplots of the *ß*-values extracted by linear models in which regional $zT1w/T2w_{mi}$ (left) and GD (right) are regressed from zFC_{G1} and stratified per Yeo-Krienen 7 network; the light grey dots represent the ρ coefficients reflecting the structure-function group-level association depicted in panel D. **H** Representation of inter-individual-level analytical dimensions. Each colour-coded slice represents a scatter plot (not shown) depicting the inter-individual relationship between S-A axis propriety (e.g., GD) and FC_{G1} for one parcel. The distribution of estimates for such relationships is depicted in panel G. $T1w/T2w_{mi}$: T1w/T2w mean intensity; GD: Geodesic Distance; FC_{G1}: Functional Connectome 1st Gradient.

We next aimed to solidify the robustness and unpack the sources of the observed associations. To do so, we further exploited the strength of the HCP design and sample, which emphasises multiple resting-state fMRI sessions (total of four sessions, ~15 min each) and includes both monozygotic (MZ) and dizygotic (DZ) twins (257 MZ, 150 women, and 153 DZ individual twins, 92 women, mean age 29 y, range=22-36 y). This allowed us to discard non-repeatable intra-individual (i.e., variance due to non-repeatable individual-level residual variance across sessions) from inter-individual differences (i.e., stable variance across sessions) and to replicate our results in a partially independent sample. Furthermore, it allowed us to differentiate amongst different sources of variability and further understand the origins of such associations. To simultaneously handle T1w/T2w$_{mi}$, GD, and FC$_{G1}$ without sacrificing interpretability for predictability [21–24], we used a Structural Equation Modeling (SEM) approach informed by the Classical Twin Design (CTD).

First, following and adapting recent advances in measurement error modelling of fMRI data [25,26], we estimated inter-individual parcel-wise variance in FC$_{G1i}$ by SEM (which we refer to as σ_{inter}^2FC$_{G1i}$). This was crucial, as large intra-individual variability can severely bias effect sizes, reduce statistical power, and increase reproducibility issues (see [21] for details). Measurement models were fitted only to one twin per pair. Estimates were obtained directly from the most likely model (Fig. 2A, see methods, see Fig. S3-S8 [27]; results replicated in models fit the other twins). Results indicate that when using individual FC$_{G1}$ extracted from four averaged ~15 min sessions (totalling ~60 min), the overall σ^2 FC$_{FCG1i}$ still contained ~33% of parcel-wise intra-individual across-sessions variability (Fig. 2B), which we were later able to partition out thanks to our approach. In contrast, the uncorrected σ^2FC$_{FCG1i}$ from a single session, which is still longer than an average rs-fMRI session included in large cohorts (e.g., UKBiobank, ~6 min [28]), contained, on average, ~61% of parcel-wise intra-individual variability. These results further illustrate the benefit of deep phenotyping strategies [21,29], implemented in the HCP as longer resting-state sessions.

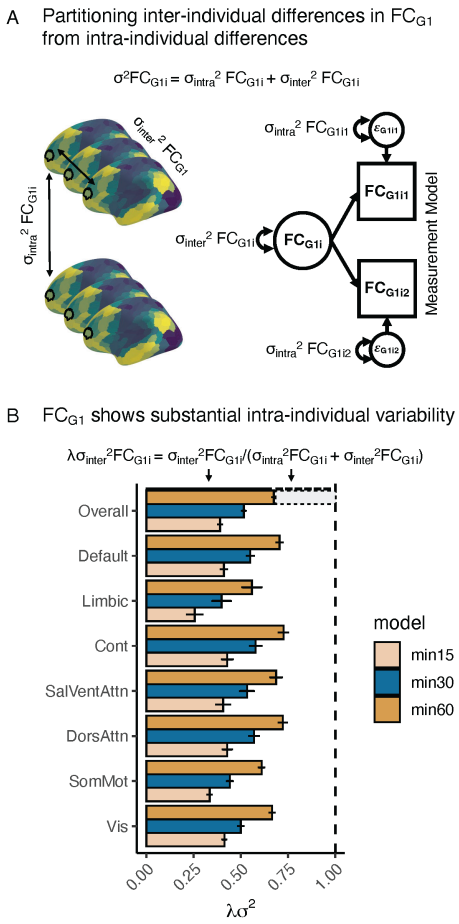

Figure 2. *Acknowledging substantial intra-individual differences in the functional S-A axis: measurement model of individual functional gradients*. **A** Conceptual and formal Structural Equation Modeling representation of the measurement model used to partition parcel-wise observed variance in individual functional gradients ($\sigma^2 FC_{G1i}$) into intra- ($\sigma_{intra}^2 FC_{G1i}$) and inter- ($\sigma_{inter}^2 FC_{G1i}$) individual variance. Squares represent the two FC_{G1i} values for a parcel *i*, obtained from individual Functional Connectomes (FC) averaged within a day (FC_{G1i1} and FC_{G1i2}, respectively). The big circle represents the latent construct capturing stable parcel-wise FC_{G1i} value. The small circles represent the day-specific FC_{G1i} values (here modelled as residuals). Double-headed arrows represent the respective variances. Single-headed arrows represent paths (all path coefficients are set to 1, and variances are directly estimated.) **B** Averaged proportion of $\sigma^2 FC_{G1}$ accounted for by $\sigma_{inter}^2 FC_{G1}$ across Yeo-Krienen functional networks and across overall parcels (overall). Colours represent averages obtained for the estimates relative to the duration of the rs-fMRI from which the FC_{G1} were obtained. FC_{G1}: Functional Connectome 1st Gradient.

To additionally get a lower bound estimate for σ_{inter}^2 in S-A structural metrics, which lack test-retest sessions, we exploited the pedigree structure of the HCP and partitioned stable genetic ($\sigma^2_{A|D}$) and unsystematic environmental sources (σ^2_E) of variability in structural S-A (T1w/T2w$_{mi}$, GD) axes. This made it possible to discard further residual sources of variance in structural metrics. Moreover, it allowed us to unpack the observed association into genetic and environmental sources of structural and functional S-A axis variation, for which we also extended the analysis to $\sigma_{inter}^2 FC_{G1i}$. We informed SEM specification of MZ and DZ twin variance-covariances of structural and functional metrics using the CTD (Fig. 3A-C). SEMs of FC_{G1} data were informed by the best-retained measurement models outlined above. Phenotypic correlations extracted by the saturated model (controlled for sex and age) of MZ and DZ pairs indicated strong genetic effects over individual variability across all metrics (Fig. 3B). Averaged MZ phenotypic correlations across parcels were all higher than DZ pair correlations (all p<.001), suggesting either ACE or ADE specification to be the most appropriate to the observed covariances. Excluding Heywood cases, we selected only models including A and E components (Fig. 3C, see methods, see Fig. S9 for power calculation). Selected models did not significantly worsen the saturated model fit (Likelihood-Ratio Test [LRT], p_{X2}>.05), were better than purely environmental E models (LRT, p_{X2}>.05), and were all within acceptable fit (CFI>.90, RMSEA <.08). This resulted in a total of 374, 289, and 305 good fitting AE parcel-wise models for T1w/T2w$_{mi}$, GD, and FC_{G1}, respectively. On average, genetic sources could account for 42%, 34%, and 56% of σ^2T1w/T2w$_{mi}$, σ^2GD, and $\sigma_{inter}^2 FC_{G1}$, respectively (twin-h^2_{mp}=.42 [sd=0.13], twin-h^2_{GD}=.34 [sd=0.09] and twin-$h^2_{interFCG1}$=.56 [sd=0.09], Fig. 3D).

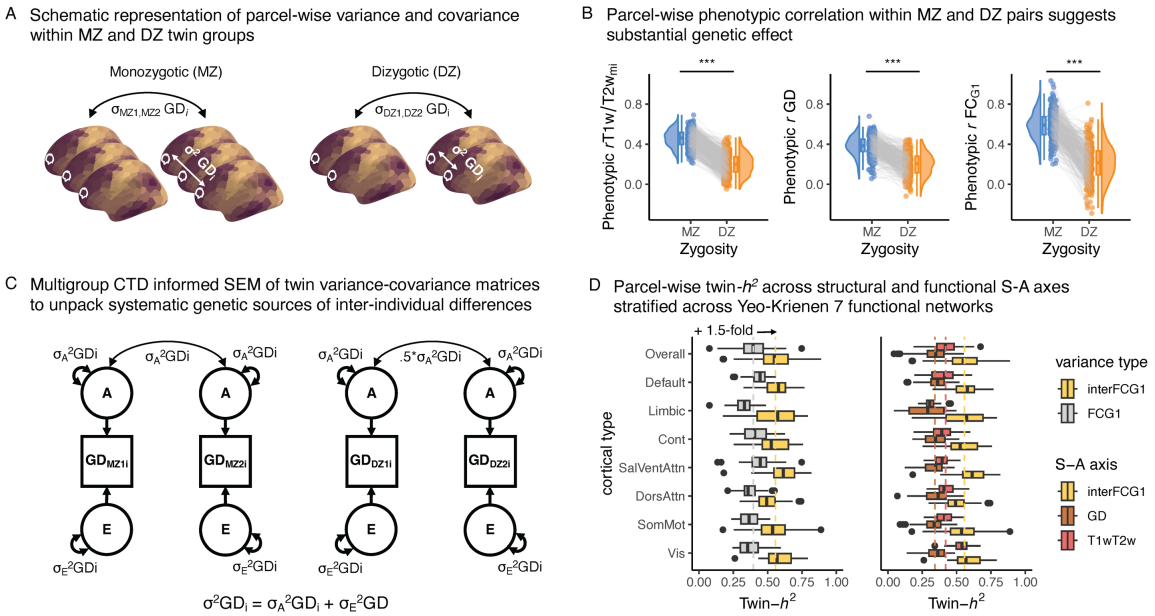

Figure 3. *Unpacking sources of individual differences in structural and functional principles of human brain organization.* **A** Graphic representation of the statistics of interest: Monozygotic (MZ) and Dyzigotic (DZ) twin variances and covariances in regional S-A axis properties. The double-headed arrow represents the covariances between MZ and DZ pairs. **B** Raincloud plots [30] of MZ and DZ twin pair phenotypic correlations extracted by the saturated model; From left to right T1w/T2w$_{mi}$, GD, and FC$_{G1}$. Each dot represents correlations per one parcel *i*, stratified by zygosity. Lines connect the same parcel. **C** Path diagram representing the univariate biometric Structural Equation Model (SEM) for GD, parcel *i* values, for both twins; Circles represent the additive (A) and environmental (E; which also contains measurement error) latent variance components. Double-edged arrows within circles represent variances; Double-edged arrows across circles represent within twin pairs covariances. All paths' coefficients (one-headed arrows) are fixed to 1. **D** Parcel-wise twin heritabilities (twin-h^2) for T1w/T2w$_{mi}$; GD, and FC$_{G1}$. Left, in light grey box-plots of the twin-h^2 for σ^2FC$_{G1;}$ in yellow, twin-h^2 σ_{inter}^2FC$_{G1;}$ Top shows the fold increase in twin-h^2 when accounting for σ_{intra}^2FC$_{G1.}$ Right, box-plots of the twin-h^2 for different S-A axis metrics; dashed lines represent the means across the entire cortex per variance type (left, intra+inter and inter only) and S-A axis (right). T1w/T2w$_{mi}$: T1w/T2w mean intensity; GD: Geodesic Distance; FC$_{G1}$: Functional Connectome 1st Gradient; A: Additive Genetic effect; E: Unique Environmental effect.

Having finally quantified both inter-individual genetic and environmental univariate sources of variability, we replicated our primary analysis (Fig. 4A). We specified a multigroup multivariate multimodal (MMM) Cholesky SEM with only A and E components (Fig. 4B). This allowed us to simultaneously discard intra-individual variability and to unpack structure-function S-A axis relationships into genetic or environmental sources. Notwithstanding relatively high twin-h^2 for both T1w/T2w$_{mi}$ and FC$_{G1}$, in the multivariate model specified on T1w/T2w$_{mi}$ data (352 parcels with satisfactory fit indices CFI>.90, RMSEA <.08), we found no significant paths between A$_{T1w/T2wmi}$ and FC$_{G1,}$ with only less than 1% of the remaining environmental paths influencing inter-individual differences in FC$_{G1}$. Conversely, for the MMM specified on GD data, (325 parcels with satisfactory fit indices, CFI>.90, RMSEA <.08), we found 46% regional GD effects over inter-individual differences in FC$_{G1}$, of which 32 indicated shared genetic effects, and 111 indicated shared environmental effects (all p<.05, Bonferroni corrected, Fig. 4C-D). Crucially, 94% of these regional effects overlapped with associations discovered in our primary analysis. Moreover, also in line with Cheverud's conjecture, which proposes that genetic correlations can approximate phenotypic ones [31–33], genetic effects over stable FC$_{G1}$ regional variability observed in the twin sample partially resembled observed phenotypic association in the primary sample, with a Spearman-rank between genetic paths and phenotypic β of ρ=.82, p<.001 (see Fig. S10). Thus, consistent with the main findings, these results show that regional structure-function relationships in the S-A axis of cortical organization between individuals can follow different trends from group-level ones.

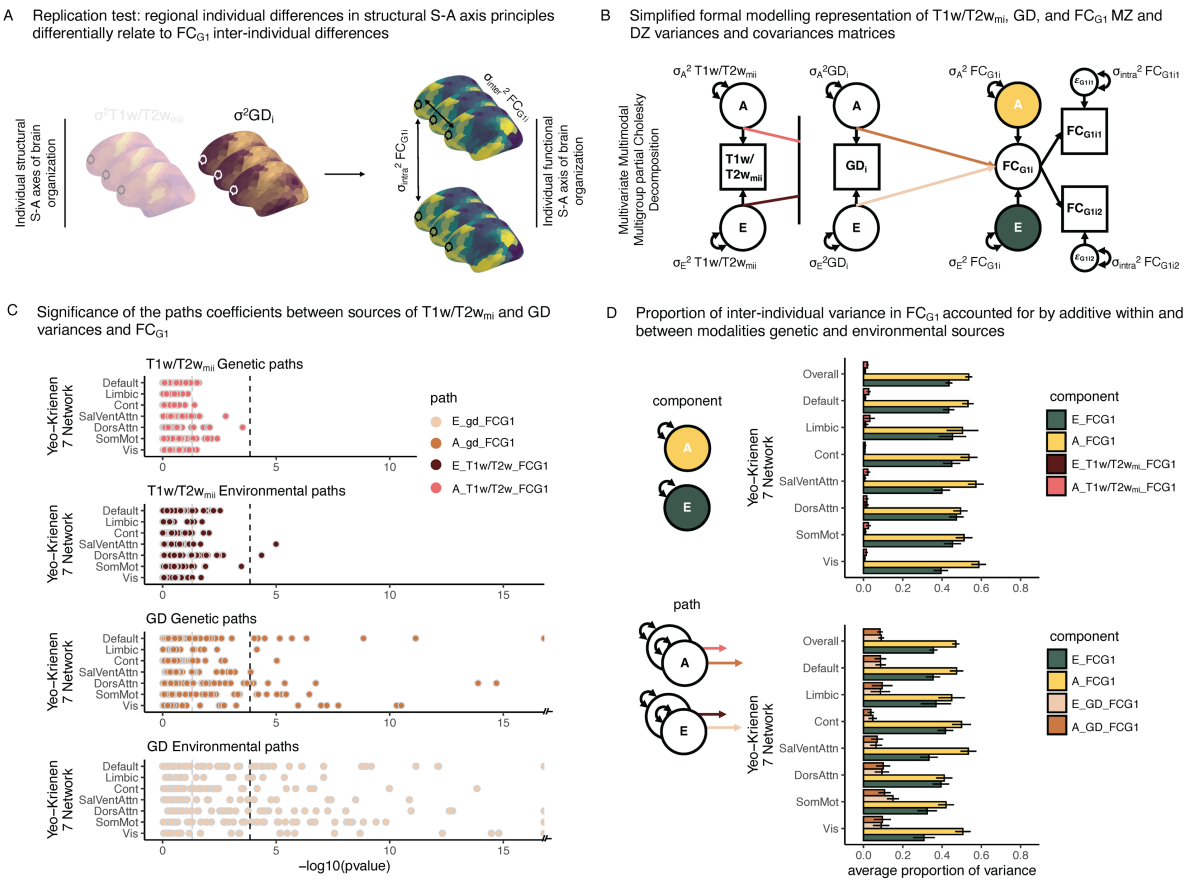

Figure 4. *Robust replication: regional differences in geodesic connectivity distances, rather than microstructure, influence inter-individual differences in the S-A cortical axis of functional connectivity.* **A** Graphic representation of the replication effort: inter-individual differences in the functional S-A axis follow cortical network geometry, as indexed by GD, S-A axis alterations. **B** Simplified representation of the Multivariate Multimodal Multigroup (MMM) Cholesky twin Model. MMM are fit to T1w/T2w$_{mi}$ values independently. To aid interpretability, estimated paths and variance components of interest are colour coded. Black paths are set to 1, and variances are directly estimated. **C** Significance of the genetic (upper) and environmental (lower) path coefficients, stratified per Yeo-Krienen network. On the top, the model fits to T1w/T2w$_{mi}$ twin data; on the bottom, the models fit to GD twin data. The dashed grey lines represent nominal significance (α=.05); The dashed black lines represent the threshold for Bonferroni-corrected significance. X-axis upper limit is set to the lavaan default, p=1*10^{-16}. **D** Bar-plots representing the averaged parcel-wise proportion of inter-FC$_{G1}$ variance (σ_{inter}^2FC$_{G1}$) explained by the A component (Additive genetic; i.e., twin-h^2), and the E component (Environmental), after accounting for the genetic and environmental paths originating from the structural metrics (e.g., A_GD_FCG1, A_GD_FCG1, for the model fit to GD data), stratified per functional network. Upper panel, the models fit to T1w/T2w$_{mi}$ twin data; lower panel, the models fit to GD twin data. Error bars represent the 95% Confidence Intervals of the mean values.; T1w/T2w$_{mi}$: T1w/T2w mean intensity; GD: Geodesic Distance; FC$_{G1}$: Functional Connectome 1st Gradient; A: Additive Genetic effect; E: Unique Environmental effect.

Finally, since regional inter-individual differences can mask global differences driving variability in the S-A axis, we extended our analysis to brain-wide estimates. We quantify T1w/T2w$_{mi}$, GD, and FC$_{G1}$ Similarity Indices (SI, Fig. 5A, see methods). We then fit an identically specified MMM SEM to the one fitted to parcel-wise data (i.e., Fig 4B) to the SI data. Source of brain-wide differences in GD accounted for by 45% of the total twin-h^2 (twin-h^2-inter-SI$_{FCG1}$=.66) and 78% of the residual brain-wide σ_{inter}FC$_{G1}^2$ (Fig. 5B). Similarly to parcel-wise estimates, brain-wide results indicated substantial overlap between genetic and environmental sources in SI of network geometry and functional organization, rather than microstructural differences, further strengthening our previous findings. These results were not explained by Intra-Cranial Volume (ICV) as a possible common cause of GD and FC$_{G1}$ SI variability (CFI<.90, RMSEA>.08; all p>.05, uncorrected, Fig. 5C-D).

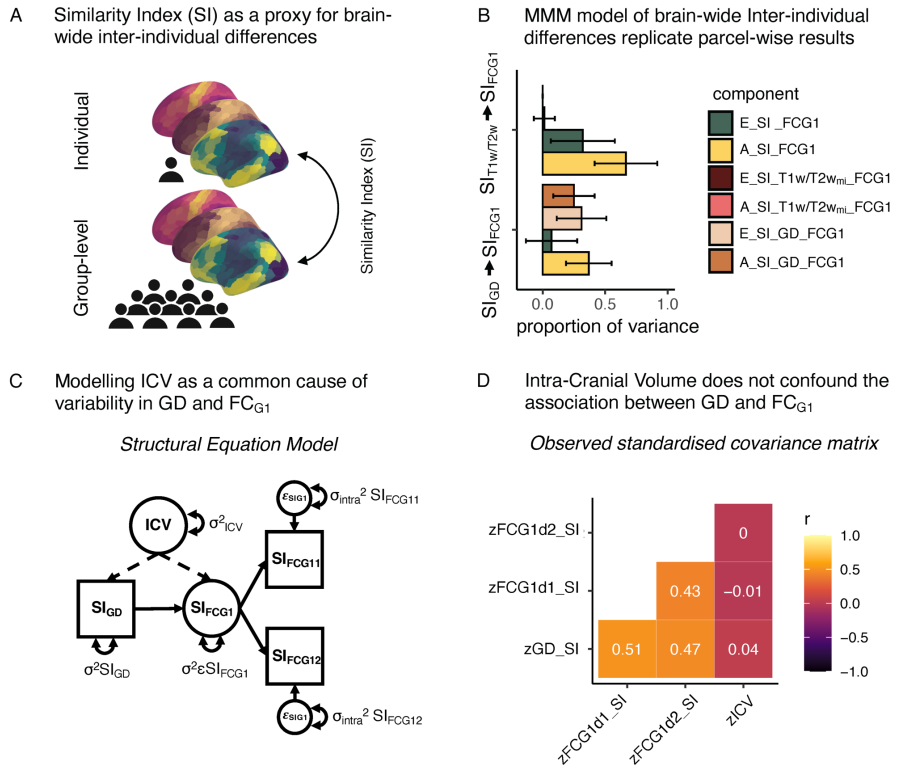

Figure 5. *Sensitivity analyses extend conclusions to brain-wide metrics and discount the effects of intra-cranial volume as a possible common cause.* **A** Graphic representation of the Similarity Index (SI) as a proposed metric to explore brain-wide inter-individual differences in the S-A axis. **B** Bar-plots representing the brain-wide proportion of $\sigma_{inter}FC_{G1}^2$ explained by the A component (Additive genetic; i.e., twin-h^2), and the E component (Environmental), after accounting for the genetic and environmental paths originating from the SI structural metrics (e.g., A_SI_GD_FCG1, A_SI_GD_FCG1, for the model fit to GD data). Error bars represent the 95% Confidence Intervals directly extracted from the structural model. **C** Formal representation of the SEM including a possible confounders, Intra-Cranial Volume (ICV). **D** Observed correlation matrix of the relationship between ICV and all SI of GD and FC_{G1}. SI: Similarity Index; MMM: Multivariate Multimodal Multigroup Cholesky decomposition; $T1w/T2w_{mi}$: T1w/T2w mean intensity; GD: Geodesic Distance; FC_{G1}: Functional Connectome 1st Gradient; ICV: Intracranial Volume.

Overall, we parsed out intra to inter-individual differences in cortical microstructural, network geometry, and intrinsic functional prosperity along the S-A axis and unpacked the origins of their associations. By doing so, we revealed that previously reported group-level associations in the S-A axis can mask pervasive inter-individual differences. Notwithstanding theoretical models and group-level relationships between cortical microstructure ($T1w/T2w_{mi}$) and intrinsic function, we found rather strong evidence that individual-level differences in regional cortical network geometry (as measured by the Geodesic Distance of inter-connected regions across the cortical mantle: GD) both phenotypically and genetically correlated with inter-individual differences in the major axis of functional connectivity (FC_{G1}). This observation aligns well with notions on the relationship between cortical connectivity distance and intrinsic and task-based functional organization [1,7,10,14,34]. In sum, our findings provide evidence that substantial inter-individual variations within and between different modalities can be overshadowed by group-level findings and emphasize the heterogeneity of genetic and environmental origins of individual variation in S-A axis cortical structure and intrinsic function. By underscoring the importance of pervasive individual differences and their origins, these results highlight the complex interplay between the structural and intrinsic functional proprieties of the S-A axis and, ultimately, the potential differential role they may play in shaping cognition [19,35–37].

Methods

Sample

We used data from the Human Connectome Project (HCP) S1200 release. The HCP includes data from 1206 individuals (656 women) that comprise 298 Monozygotic (MZ) twins, 188 Dizygotic (DZ) twins, and 720 singletons, with mean age ± *sd*=28.8 ± 3.7 years (age range=22-37 years). Informed consent for all individuals was obtained by HCP, and our data usage was approved by HCP and complied with all relevant ethical regulations for working with human participants (see [11,17,38]). The primary participant pool comes from individuals born in Missouri to families that include twins, sampled as healthy representatives of ethnic and socioeconomic diversity of US individuals, based on data from the Missouri Department of Health and Senior Services Bureau of Vital Records. We followed standard guidelines for inclusion criteria as described elsewhere[11]. Our final sample comprised 1001 individuals, including 257 MZ, 150 women, and 153 DZ individual twins, 92 women, mean age 29, range=22-36 y. We included only twins where we confirmed genotyped zygosity.

Functional Imaging

Functional connectivity matrices were based on four 14 min 33 s of functional Magnetic Resonance Imaging (fMRI) data acquired over two sessions, spaced two days apart, through the HCP, which underwent HCP's minimal preprocessing. For each individual, four functional connectivity matrices were computed using the minimally preprocessed, spatially normalised resting-state fMRI (rs-fMRI) scans, which were co-registered using MSMAll to template HCP 32k_LR surface space. 32k_LR surface space consists of 32,492 total nodes per hemisphere (59,412 excluding the medial wall). We computed four functional connectivity (FC) matrices per individual from the average time series extracted in each of the 400 Schaefer cortical parcels. The individual functional connectomes were generated by averaging preprocessed time series within nodes, Pearson correlating nodal time series and converting them to Fisher-z scores. The average FC was obtained by averaging FCs within individuals (i.e., between sessions) and between individuals.

Structural imaging

MRI protocols of the HCP have been previously described [17,38]. MRI data were acquired originally on the same day on the HCP's custom 3T Siemens Skyra equipped with a 32-channel head coil. T1w images with identical parameters were acquired using a 3D-MP-RAGE sequence over 7 min 40 s (0.7 mm isovoxels, matrix = 320 × 320, 256 sagittal slices; TR = 2400 ms, TE = 2.14 ms, TI = 1000 ms, flip angle = 8°; iPAT = 2). T2w images were acquired using a 3D T2-SPACE sequence with identical geometry over 8 min and 24 s (TR = 3200 ms, TE = 565 ms, variable flip angle; iPAT = 2). We followed preprocessing steps outlined in Valk et al. [11].

Parcellation and Functional Networks

We used the Schaefer group-level hard-parcellation, originally obtained by a gradient-weighted Markov random field model integrating local gradient and global similarity approaches [18]. To stratify results within established cortical functionally coupled networks, we used the seven Yeo-Krienen networks [39].

Microstructural profiles: $T1w/T2w_{mi}$

We used T1w/T2w imaging myelin-sensitive contrast from the HCP minimal processing pipeline, which uses the T2w to correct for inhomogeneities in the T1w image to estimate mean intensity T1w/T2w microstructural profiles ($T1w/T2w_{mi}$). $T1w/T2w_{mi}$ has been shown to map to model-based tract-tracing histological data in macaque, estimate intracortical myelin content, and thus approximate architectural complexity and cortical hierarchy [8].

Geodesic distance: GD

Individual Geodesic Distances (GD) were computed using the Micapipe toolbox [40]. Briefly, we computed GD between each region and their top 10% of maximally functionally connected regions along each individual native cortical midsurface. We further averaged within regions to obtain a parcel-wise value and improve computation performance. Micapipe implements the Dijkstra algorithm [41] (further details can be found in [40]).

S-A functional axis: FC_{G1}

We sequentially averaged FCs, first within days, resulting in two FCs per individual, and then between days, resulting in one FC per individual. We then extracted six first components from the four not averaged, two sequentially averaged and one averaged FCs, using the python package BrainSpace [42]. Extraction of the first eigenvector followed standard procedures, with the original individual FCs set at a connection density of 10% (i.e., the FCs were made sparse by setting a sparsity threshold of 90%). The first ten eigenvectors were then obtained by decomposing the FCs by diffusion map embedding, a robust non-linear manifold learning technique. To aid comparability across individuals, we aligned individual eigenvectors to the template eigenvector by Procrustes rotation [43] (results with unaligned individual FC_{G1} can be found in Fig. S2). The template functional gradient was directly extracted from the overall mean FC matrix.

Associations analysis

First, we computed Spearman rank-order correlations between the structural ($T1w/T2w_{mi}$ and GD) and functional (FC_{G1}) S-A axis group-level modalities. We then expanded analysis to regional individual differences and fit linear models where each parcel-wise FC_{G1} was regressed on either $T1w/T2w_{mi}$ or GD. Signficance was evaluated after Bonferroni correction for multiple comparisons.

Measurement model of error in individual variability of the functional S-A axis

To partition stable between-individual variability in parcel-wise G1, we applied Structural Equation Modeling (SEM), adapting previously retained measurement error models to rs-fMRI to gradients [25,26]. First, we fit two measurement models (test-retest-2) to parcel-wise G1 data averaged across days, one without restrictions and one with restricted residuals. We then fit six measurement models to the parcel-wise G1 obtained from each ~15min rs-fMRI session (test-retest-4). Each model is nested compared to the complex unrestricted model. Five out of six test-retest-4 models included an additional Session (S) component, capturing a hypothetical stable between-individual parcel-wise G1 variance unique to the day of the scanning session (see Fig. S4). We then used multimodel rank-based Akaike Information Criteria (AIC) inference to compare the relative fit between the two test-retest-2 and the six test-retest-4 models across all 400 parcels. We first rank the model across parcels from the lowest to the highest AIC; we subtract each AIC from the lowest possible AIC (ΔAIC). We inspected the histogram of the ΔAIC per model and retained the models that reflected best the multimodel inference cutoff of $\Delta AIC<2$ (acceptable) $\Delta AIC>10$ (poor)[27]. Selected measurement models were used for the later Structural Models of genetic and environmental variance (see Fig. S5-S6). Further, we used model estimates to compute the parcel-wise averaged proportion of stable between-person variance in G1 captured by each single and within-day averaged FC following canonical path tracing rules (see Fig. S7). We used Spearman-brown correction to estimate the stable between-person G1 variance obtained by averaging the 4 FCs. We validate our analysis by comparing estimates extracted by the model with Intra-class Correlation Coefficients (ICC) [44], type 2 and 2k, respectively (ICC(2,1) and ICC(2,k)) and provide them in the supplementary (see Fig. S8).

Twin-based Structural Equation Modeling

We used multigroup Structural Equation Modeling (SEM) to partition parcel-wise variability in structural ($\sigma^2 T1w/T2w_{mii}$, $\sigma^2 GD_i$) and functional ($\sigma_{inter}{}^2 FC_{G1i}$) S-A modalities into either

additive genetic (σ^2_A) or non-additive genetics (σ^2_D), common (σ^2_C) and unsystematic environemntal (σ^2_E) sources of variance. SEMs were fit to Individual twins parcel-wise σ^2T1w/T2w$_{mii}$, σ^2GD$_i$, and σ^2FC$_{G1i1}$ (day1) and σ^2FC$_{G1i2}$ (day 2), and between twins within zygosity covariances (See Fig. 3C). The model specification was informed by the Classical Twin Design [45]. Briefly, MZ twins are ~100 % genetically identical, coming from the same fertilised egg. In contrast, DZ twins are, on average, only 50% additively and 25% non-additively genetically similar, in regards to allelic variants, coming from two different fertilised eggs. Thus, the correlation between the additive genetic component (A) is set to be equal to 1 for MZ while .5 for DZ. The correlation between the dominance genetic component (D) is set to be equal to 1 for MZ and .25 for DZ. The common environment (C) is set to be equally shared across twins and thus equal to 1 within both types of twins. In contrast, the unique environment (E) component will be unique to each twin; therefore, their correlation will be equal to 0. In total, we fit five models for each of the five parcel-wise univariate multigroup SEM per parcel ([1+3]x1x400 models for Tw1/Tw2$_{mi}$; [1+3]x1x400 models for GD; and [1+3]x5x400 models for FC$_{G1}$, [saturated model + biometric models] x measurement model x parcel, respectively). For each model, we fit a saturated model and, based on the pattern of MZ and DZ correlation extracted by the saturated model, an ACE or an ADE, and AE, E model, as an ACDE model is under-identified. We fit an ACE model when MZ correlations were less than twice DZ correlations and an ADE if correlations were more than double. Each model was fit to both measured data without accounting for error variance; the two best test-retest-2 measurement models and the two best test-retest-4 measurement models were selected from the multimodel inference step outlined above. We employed the direct symmetric approach by estimating variance components directly while setting path coefficients to 1. We chose this approach as it has been shown to reduce type I errors and produce unbiased χ^2 [46].

Narrow-sense twin heritability (twin-h^2) estimates were defined as the ratio of the additive genetic variance over the total phenotypic variance:

$$\text{twin-}h^2 = \frac{\sigma_A^2}{\sigma_A^2+\sigma_E^2}$$

All models were fitted in Lavaan [47] without accounting for the mean structure of the data. Parameters were estimated via Maximum Likelihood with a Robust (MLR) estimator for standard error and fit indices. We validated our analyses by comparing estimates obtained in the standard statistical package OpenMx [48], both with and without mean structure, and give results for alternative estimators (see Fig. S11).

We evaluated the goodness for each parcel by both relative and absolute fit indices. First, we assessed the relative fit index of the ACE, ADE, and AE, E models, compared to the saturated model by -2log-likelihood ratio test (LRT). The LRT is asymptotically χ^2 distributed, approximately equal to the difference between the χ^2 of the most parsimonious subtracted by the least parsimonious model. Models with a $\Delta\chi^2$, with degrees of freedom equal to the difference in degrees of freedom between the two models, $p<.05$, were deemed to worsen the model fit and thus not selected. Parcels for which the biometric model fit was worse than the saturated model were not considered for further analysis. Given the use of a direct symmetric approach, we additionally restricted selected models which were found to be Heywood cases (i.e., negative variances or correlations higher than one [46]). Selected models were further evaluated for their absolute fit by Comparative Fit Index (CFI) and Root Mean Square Error of Approximation (RMSEA). Following standard cutoffs, we retained only models with a "satisfactory" CFI >.90 and an RMSEA<.08. For G1, the final model across all parcels was selected based on two criteria: average fold-increase in twin-h^2 estimates compared to the model not accounting for measurement error and the overall number of parcels passing the relative and absolute fit cutoffs.

The final models were then re-run on the residualised T1w/T2w$_{mii}$, GD$_i$, and FC$_{G1i}$ controlled for the sex and the age of the individuals. The averaged MZ and DZ correlations were obtained by Fisher *z*-transforming the extracted phenotypic correlations from such best-

selected saturated model and transforming the *z* back to *r*. Similarly, the operations computed on the phenotypic correlations were carried out on the z-transformed values.

Multivariate Multimodal Multigroup Cholesky Structural Equation Modelling

We specified a Multivariate Multimodal Multigroup (MMM) Cholesky SEM of MZ and DZ parcel-wise T1w/T2w$_{mi,}$ GD, and FC$_{G1}$ data. After the procedures described above, the measurement model accounting for intra-individual variability in FC$_{G1}$ was selected (multimodal ranked AIC inference, LRT, CFI and RMSEA). We estimated variance components directly and set all path coefficients to 1, except for the ones originating from structural modalities to FC$_{G1.}$ This allowed us to freely estimate the contribution of genetic and environmental effects over variability in T1w/T2w$_{mi}$ to variability in parcel-wise error-free estimates for inter-FC$_{G1}$. As a consequence of the model specification, the A and E components for the inter-FC$_{G1}$ now reflect genetic and non-genetic effects over variability in parcel-wise inter-individual unsystematic error-free FC$_{G1}$ estimates after accounting for genetic and not genetic-effects shared with T1w/T2w$_{mi}$ or GD. For example, for the model including GD and FC$_{G1}$, the total amount of repeatable variance in any parcel FC$_{G1i}$ is now decomposed into:

$$\sigma^2_{interFCG1i} = \sigma^2_{AFCG1i} + \sigma^2_{EFCG1i} + \gamma^2_{AGD\_FCG1i} * \sigma^2_{AGDi} + \gamma^2_{EGDi\_FCG1i} * \sigma^2_{EGDi}$$

The direct relative contribution of each additive and genetic source can be calculated, following the pathway tracing rule, as follows:

$$A_{FCG1i} = \frac{\sigma^2_{AFCG1i}}{\sigma^2_{interFCG1i}}$$

$$E_{FCG1i} = \frac{\sigma^2_{EFCG1i}}{\sigma^2_{interFCG1i}}$$

$$A_{GD\_FCG1i} = \frac{\gamma^2_{AGD\_FCG1i} * \sigma^2_{AGDi}}{\sigma^2_{interFCG1i}}$$

$$E_{GD\_FCG1i} = \frac{\gamma^2_{EGD\_FCG1i} * \sigma^2_{EGDi}}{\sigma^2_{interFCG1i}}$$

Similar to what was reported above, models were fitted in Lavaan using the MLR estimator. To improve interpretability, we standardized parcel-wise values before model fitting.

Sensitivity analysis

We quantified T1w/T2w$_{mi}$, GD, and FC$_{G1}$ Similarity Indices (SI). We obtained the SI by correlating each individual T1w/T2w$_{mi}$, GD or FC$_{G1}$ vector with respective S-A group-level modality vectors. For example, SI$_{GDj}$ for an individual *j* was obtained by correlating their GD with the group-level GD. Similarly, for the same individual *j*, SI$_{FCG1j}$, was obtained by correlating their FC$_{G1}$ at day 1 and at day 2 of scanning with the group-level FC$_{G1}$. Similar to what is outline above for parcel-wise analysis, we went on to fit a measurement model to each SI FC$_{G1i1}$ and FC$_{G1i2}$ value. We then specified the same MMM Cholesky model and fit it to FC$_{G1i1,}$ FC$_{G1i2,}$ and either T1w/T2w$_{mi}$ or GD SI data. To discount for possible whole brain volumetric confounding effects, we specified a SEM where variation in Intracranial Volume was assumed to act as a common cause of GD and FC$_{G1}$ differences and fit it accordingly to GD, FC$_{G1i1,}$ and FC$_{G1i2}$ SI data.

Data availability

We obtained human data from the open-access Human Connectome Project HCP S1200 young adult sample. Data are available upon request at http://www.humanconnectome.org/.

Code availability

All code will be available upon publication, including Lavaan scripts to compute measurement models and carry out univariate and multivariate twin analyses. Code and tutorial for functional gradient decomposition are available at https://brainspace.readthedocs.io/en/latest/pages/install.html.
The code and tutorial to generate Geodesic Distance can be found at https://micapipe.readthedocs.io/en/latest/.
Structural equation modelling and twin-based analysis have been done using the statistical package https://lavaan.ugent.be/. Comparison with standard statistical packages, OpenMx https://openmx.ssri.psu.edu/, to analyze twin data have been carried out thanks to the available scripts at https://hermine-maes.squarespace.com/.

Acknowledgements

We want to thank the Human Connectome Project, Washington University, the University of Minnesota, and Oxford University Consortium (Principal Investigators: David Van Essen and Kamil Ugurbil; 1U54MH091657) originally funded by the 16 N.I.H. Institutes and Centers that support the N.I.H. Blueprint for Neuroscience Research; and by the McDonnell Center for Systems Neuroscience at Washington University. We would also like to thank Jitse Amelink, Meike D. Hettwer, and MacKenzie D. Trupp for their comments on the draft. Furthermore, we would like to thank the Max Planck School of Cognition. This study was supported by the German Federal Ministry of Education and Research (BMBF) and Max Planck Society.

Contributions

S.L.V. and G.B. conceptualized the work; S.L.V. & S.E.F. supervised the research. G.B. performed primary analyses; S.L.V., S.E.F, M.G.N, B.C.B., and R.A.I. gave input on analysis; S.L.V. performed functional connectomics, microstructural and geodesic distance analysis; H.L.S. provided input in diffusion map embedding analysis; G.B. computed figures; M.G.N gave input on Figure 1; G.B, & S.L.V. drafted the manuscript; S.L.V., S.E.F, M.G.N, B.C.B., H.L.S., and R.A.I. contributed to revising the manuscript.

Corresponding author

*Correspondence to S.L.V.; email:valk@cbs.mpg.de

References

1. Margulies, D. S. *et al.* Situating the default-mode network along a principal gradient of macroscale cortical organization. *Proc. Natl. Acad. Sci.* **113**, 12574–12579 (2016).
2. Mesulam, M. M. From sensation to cognition. *Brain* **121**, 1013–1052 (1998).
3. Sydnor, V. J. *et al.* Neurodevelopment of the association cortices: Patterns, mechanisms, and implications for psychopathology. *Neuron* **109**, 2820–2846 (2021).
4. Sydnor, V. J. *et al.* Intrinsic activity development unfolds along a sensorimotor–association cortical axis in youth. *Nat. Neurosci.* 1–12 (2023) doi:10.1038/s41593-023-01282-y.
5. Brodmann, K. ergleichende Lokalisationslehre der Grosshirnrinde in ihren Prinzipien dargestellt auf Grund des Zellenbaues. *Barth* (1909).
6. von Economo, C. F. & Koskinas, G. N. Die cytoarchitektonik der hirnrinde des erwachsenen menschen. *J Springer* (1925).
7. Ercsey-Ravasz, M. *et al.* A predictive network model of cerebral cortical connectivity based on a distance rule. *Neuron* **80**, 184–197 (2013).
8. Burt, J. B. *et al.* Hierarchy of transcriptomic specialization across human cortex captured by structural neuroimaging topography. *Nat. Neurosci.* **21**, 1251–1259 (2018).
9. Saberi, A. *et al.* The spatial arrangement of laminar thickness profiles in the human cortex scaffolds processing hierarchy. 2023.03.25.532115 Preprint at https://doi.org/10.1101/2023.03.25.532115 (2023).
10. Markov, N. T. *et al.* Cortical high-density counterstream architectures. *Science* **342**, 1238406 (2013).
11. Valk, S. L. *et al.* Genetic and phylogenetic uncoupling of structure and function in human transmodal cortex. *Nat. Commun.* **13**, 2341 (2022).
12. Demirtaş, M. *et al.* Hierarchical Heterogeneity across Human Cortex Shapes Large-Scale Neural Dynamics. *Neuron* **101**, 1181-1194.e13 (2019).
13. Paquola, C., Amunts, K., Evans, A., Smallwood, J. & Bernhardt, B. Closing the mechanistic gap: the value of microarchitecture in understanding cognitive networks. *Trends Cogn. Sci.* **26**, 873–886 (2022).

14. Pang, J. C. *et al.* Geometric constraints on human brain function. 2022.10.04.510897 Preprint at https://doi.org/10.1101/2022.10.04.510897 (2023).
15. Suárez, L. E., Markello, R. D., Betzel, R. F. & Misic, B. Linking Structure and Function in Macroscale Brain Networks. *Trends Cogn. Sci.* **24**, 302–315 (2020).
16. Huntenburg, J. M., Bazin, P.-L. & Margulies, D. S. Large-Scale Gradients in Human Cortical Organization. *Trends Cogn. Sci.* **22**, 21–31 (2018).
17. Van Essen, D. C. *et al.* The Human Connectome Project: A data acquisition perspective. *NeuroImage* **62**, 2222–2231 (2012).
18. Schaefer, A. *et al.* Local-Global Parcellation of the Human Cerebral Cortex from Intrinsic Functional Connectivity MRI. *Cereb. Cortex* **28**, 3095–3114 (2018).
19. Hong, S.-J. *et al.* Atypical functional connectome hierarchy in autism. *Nat. Commun.* **10**, 1022 (2019).
20. Bernhardt, B. C., Smallwood, J., Keilholz, S. & Margulies, D. S. Gradients in brain organization. *NeuroImage* **251**, 118987 (2022).
21. Tiego, J. *et al.* Precision behavioral phenotyping as a strategy for uncovering the biological correlates of psychopathology. *Nat. Ment. Health* **1**, 304–315 (2023).
22. Genon, S., Eickhoff, S. B. & Kharabian, S. Linking interindividual variability in brain structure to behaviour. *Nat. Rev. Neurosci.* **23**, 307–318 (2022).
23. Willoughby, E. A., Polderman, T. J. C. & Boutwell, B. B. Behavioural genetics methods. *Nat. Rev. Methods Primer* **3**, 1–16 (2023).
24. Hagenbeek, F. A. *et al.* Maximizing the value of twin studies in health and behaviour. *Nat. Hum. Behav.* 1–12 (2023) doi:10.1038/s41562-023-01609-6.
25. Teeuw, J., Hulshoff Pol, H. E., Boomsma, D. I. & Brouwer, R. M. Reliability modelling of resting-state functional connectivity. *NeuroImage* **231**, 117842 (2021).
26. Brandmaier, A. M. *et al.* Assessing reliability in neuroimaging research through intra-class effect decomposition (ICED). *eLife* **7**, e35718 (2018).
27. Maes, H. H., Neale, M. C., Kirkpatrick, R. M. & Kendler, K. S. Using Multimodel Inference/Model Averaging to Model Causes of Covariation Between Variables in Twins. *Behav. Genet.* **51**, 82–96 (2021).

28. Marek, S. *et al.* Reproducible brain-wide association studies require thousands of individuals. *Nature* **603**, 654–660 (2022).
29. Friedman, N. P., Banich, M. T. & Keller, M. C. Twin studies to GWAS: there and back again. *Trends Cogn. Sci.* **25**, 855–869 (2021).
30. Allen, M., Poggiali, D., Whitaker, K., Marshall, T. R. & Kievit, R. A. Raincloud plots: a multi-platform tool for robust data visualization. *Wellcome Open Res.* **4**, 63 (2019).
31. van Rheenen, W., Peyrot, W. J., Schork, A. J., Lee, S. H. & Wray, N. R. Genetic correlations of polygenic disease traits: from theory to practice. *Nat. Rev. Genet.* **20**, 567–581 (2019).
32. Sodini, S. M., Kemper, K. E., Wray, N. R. & Trzaskowski, M. Comparison of Genotypic and Phenotypic Correlations: Cheverud's Conjecture in Humans. *Genetics* **209**, 941–948 (2018).
33. Warrier, V. *et al.* The genetics of cortical organisation and development: a study of 2,347 neuroimaging phenotypes. 2022.09.08.507084 Preprint at https://doi.org/10.1101/2022.09.08.507084 (2022).
34. Langdon, C., Genkin, M. & Engel, T. A. A unifying perspective on neural manifolds and circuits for cognition. *Nat. Rev. Neurosci.* **24**, 363–377 (2023).
35. Dong, D. *et al.* Compressed sensorimotor-to-transmodal hierarchical organization in schizophrenia. *Psychol. Med.* **53**, 771–784 (2023).
36. Xia, M. *et al.* Connectome gradient dysfunction in major depression and its association with gene expression profiles and treatment outcomes. *Mol. Psychiatry* **27**, 1384–1393 (2022).
37. Liu, S., Smit, D. J. A., Abdellaoui, A., van Wingen, G. A. & Verweij, K. J. H. Brain Structure and Function Show Distinct Relations With Genetic Predispositions to Mental Health and Cognition. *Biol. Psychiatry Cogn. Neurosci. Neuroimaging* **8**, 300–310 (2023).
38. Glasser, M. F. *et al.* The minimal preprocessing pipelines for the Human Connectome Project. *NeuroImage* **80**, 105–124 (2013).
39. Yeo, B. T. T. *et al.* The organization of the human cerebral cortex estimated by intrinsic functional connectivity. *J. Neurophysiol.* **106**, 1125–65 (2011).

40. Cruces, R. R. *et al.* Micapipe: A pipeline for multimodal neuroimaging and connectome analysis. *NeuroImage* **263**, 119612 (2022).
41. Dijkstra, E. W. A note on two problems in connexion with graphs. *Numer. Math.* **1**, 269–271 (1959).
42. Vos de Wael, R. *et al.* BrainSpace: a toolbox for the analysis of macroscale gradients in neuroimaging and connectomics datasets. *Commun. Biol.* **3**, 1–10 (2020).
43. Bethlehem, R. A. I. *et al.* Dispersion of functional gradients across the adult lifespan. *NeuroImage* **222**, 117299 (2020).
44. Koo, T. K. & Li, M. Y. A Guideline of Selecting and Reporting Intraclass Correlation Coefficients for Reliability Research. *J. Chiropr. Med.* **15**, 155–163 (2016).
45. Boomsma, D., Busjahn, A. & Peltonen, L. Classical twin studies and beyond. *Nat. Rev. Genet.* **3**, 872–882 (2002).
46. Verhulst, B., Prom-Wormley, E., Keller, M., Medland, S. & Neale, M. C. Type I Error Rates and Parameter Bias in Multivariate Behavioral Genetic Models. *Behav. Genet.* **49**, 99–111 (2019).
47. Rosseel, Y. lavaan: An R Package for Structural Equation Modeling. *J. Stat. Softw.* **48**, 1–36 (2012).
48. Neale, M. C. *et al.* OpenMx 2.0: Extended Structural Equation and Statistical Modeling. *Psychometrika* **81**, 535–549 (2016).